JGR Space Physics

RESEARCH ARTICLE
10.1029/2018JA025726

Special Section:
The Earth's Magnetosphere: New Tools, New Thinking, New Results

Investigating Loss of Relativistic Electrons Associated With EMIC Waves at Low *L* Values on 22 June 2015

Murong Qin[1], Mary Hudson[1], Zhao Li[1], Robyn Millan[1], Xiaochen Shen[2], Yuri Shprits[3,4,5], Leslie Woodger[1], Allison Jaynes[6], and Craig Kletzing[6]

[1]Department of Physics and Astronomy, Dartmouth College, Hanover, NH, USA, [2]Center for Space Physics, Boston University, Boston, MA, USA, [3]GFZ German Research Centre for Geosciences, Potsdam, Germany, [4]Institute of Physics and Astronomy, University of Potsdam, Potsdam, Germany, [5]Department of Earth, Planetary, and Space Sciences, University of California, Los Angeles, CA, USA, [6]Department of Physics and Astronomy, University of Iowa, Iowa City, IA, USA

Abstract In this study, rapid loss of relativistic radiation belt electrons at low L^* values (2.4–3.2) during a strong geomagnetic storm on 22 June 2015 is investigated along with five possible loss mechanisms. Both the particle and wave data are obtained from the Van Allen Probes. Duskside H^+ band electromagnetic ion cyclotron (EMIC) waves were observed during a rapid decrease of relativistic electrons with energy above 5.2 MeV occurring outside the plasmasphere during extreme magnetopause compression. Lower He^+ composition and enriched O^+ composition are found compared to typical values assumed in other studies of cyclotron resonant scattering of relativistic electrons by EMIC waves. Quantitative analysis demonstrates that even with the existence of He^+ band EMIC waves, it is the H^+ band EMIC waves that are likely to cause the depletion at small pitch angles and strong gradients in pitch angle distributions of relativistic electrons with energy above 5.2 MeV at low *L* values for this event. Very low frequency wave activity at other magnetic local time can be favorable for the loss of relativistic electrons at higher pitch angles. An illustrative calculation that combines the nominal pitch angle scattering rate due to whistler mode chorus at high pitch angles with the H^+ band EMIC wave loss rate at low pitch angles produces loss on time scale observed at $L = 2.4$–3.2. At high *L* values and lower energies, radial loss to the magnetopause is a viable explanation.

Key Points:
- Greater than 5.2-MeV electron loss predominantly occurs outside the plasmasphere during the extreme magnetopause compression event on 22 June 2015
- Relativistic electron loss is colocated with H^+ band EMIC waves at low *L*
- Five possible loss mechanisms are considered to explain the fast net loss of relativistic electrons, including H^+ EMIC wave scattering

Correspondence to:
M. Qin,
murong.qin.gr@dartmouth.edu

Citation:
Qin, M., Hudson, M. K., Li, Z., Millan, R. M., Shen, X.-C., Shprits, Y. Y., et al. (2019). Investigating loss of relativistic electrons associated with EMIC waves at low *L* values on 22 June 2015. *Journal of Geophysical Research: Space Physics*, *124*, 4022–4036. https://doi.org/10.1029/2018JA025726

Received 30 MAY 2018
Accepted 29 APR 2019
Accepted article online 6 MAY 2019
Published online 5 JUN 2019

1. Introduction

The evolution of the electron fluxes in the Earth's outer radiation belt, dominated by competing source and loss processes, can be highly variable (Reeves et al., 2003; Shen et al., 2017). There are three main mechanisms that can cause decrease in flux: (1) the Dst effect, (2) radial loss to the magnetopause, and (3) precipitation into the loss cone (e.g., Millan & Thorne, 2007; Millan et al., 2010). Among the three mechanisms, the Dst effect is an adiabatic change of the radiation belt electron flux; that is, the electrons drift outward to conserve the third adiabatic invariant when the geomagnetic field decreases due to buildup of the ring current during the main phase of geomagnetic storms and then drift back toward the earth during the recovery phase (Kim & Chan, 1997). Without any other addition or loss process, there is no net loss if the magnetic field relaxes to prestorm conditions. The other two are real loss mechanisms. Radial loss to the magnetopause includes magnetopause shadowing and outward radial transport processes. Magnetopause shadowing occurs when the magnetopause is compressed by solar wind dynamic pressure, and electrons can be lost directly to the magnetopause if their drift path crosses the boundary of the magnetosphere (Li et al., 2015), resulting in a sharp negative gradient in phase space density (PSD) along increasing radial distance. Outward diffusion driven by the sharp gradient in PSD and ultralow frequency waves can further drive the loss to the magnetopause (Hudson et al., 2014; Shprits et al., 2006; Turner et al., 2012). Radiation belt electrons can also be scattered into the atmospheric loss cone through interaction with various modes of plasma waves, including whistler mode chorus, whistler mode hiss, and electromagnetic ion cyclotron (EMIC) waves (e.g., Capannolo et al., 2018, 2019; Li et al., 2014; Qin et al., 2018; Summers et al., 2007; Su et al., 2017). EMIC waves have been shown not only to produce loss at small pitch angles (Usanova et al., 2014) but also to initialize the fast net loss at all pitch angles when whistler mode waves are there to transport electrons from near 90° pitch angles toward the loss cone with strong gradients in pitch angles generated by

EMIC wave-driven loss (Drozdov et al., 2017; Li et al., 2007; Ma et al., 2015; Mourenas et al., 2016; Shprits et al., 2016; Zhang et al., 2017).

Previous studies have shown that He^+ band EMIC waves are more likely to exist in the high-density region, inside the plasmasphere and plumes, while the H^+ band EMIC waves usually grow in the low-density region (Denton et al., 2014), thought to be less favorable for EMIC waves to interact with relativistic electrons due to minimum resonant energy discussed below (Summers & Thorne, 2003). Thus, less attention has been paid to H^+ band EMIC waves when investigating EMIC wave-driven precipitation of relativistic electrons. However, the efficiency of EMIC waves in scattering relativistic electrons is influenced by complex factors, such as initial distributions of radiation belt electron fluxes, wave amplitude, the wave frequency in each propagation band, and background plasma parameters. The minimum energy for electrons to interact with H^+ band EMIC waves can be lower than He^+ band EMIC waves depending on the wave properties and plasma parameters in the region of occurrence. Qin et al. (2018) found that the proportion of H^+ band EMIC wave events that are associated with relativistic electron precipitation is even slightly higher than for He^+ band EMIC wave activity.

In previous studies, cold ion composition is adopted with typical assumed values since direct measurement of low energy ions is affected by the spacecraft potential and cannot be detected down to lowest energies (Min et al., 2015). However, the minimum resonant energy and pitch angle diffusion coefficient are sensitive to the cold ion composition (Summers & Thorne, 2003; Uzbekov et al., 2016), which varies with geomagnetic activity and location in the magnetosphere (Denton et al., 2014). Thus, it is important to have a more accurate value of the cold ion composition.

In our study, we report observations of a loss of relativistic electrons during an extreme magnetopause compression event on 22 June 2015. The electron flux drop with energy below 5.2 MeV at high L values was explained with magnetopause shadowing (Xiang et al., 2017). We focus analysis on the loss of relativistic electrons (>5.2 MeV) at low L values that is strongly correlated in time and space with H^+ band EMIC waves observed outside a highly compressed plasmasphere. The minimum resonant energy and a pitch angle diffusion coefficient for relativistic electrons to interact with EMIC waves have been calculated. We improve on previous applications of quasi-linear theory by incorporating realistic cold plasma composition calculated from the stop band cutoff frequencies measured by the wave instrument on Van Allen Probes.

In section 2, the behavior of electron flux drop in different energy channels is compared. We focus on the flux drop at low L^* (Tsyganenko & Sitnov, 2005) values at higher energies and present concurrent observation of EMIC wave activity. In section 3, five possible loss mechanisms are considered: radial loss to the magnetopause, pitch angle scattering by whistler mode waves, such as chorus, hiss, or hiss in plumes, H^+ band EMIC wave-driven loss through bounce resonance, H^+ band EMIC wave-driven loss due to cyclotron resonance, and pitch angle scattering by combined effects of EMIC waves and chorus waves. Detailed analysis of the minimum resonant energy is presented along with the pitch angle diffusion coefficient and resulting estimate of loss time scale for electrons cyclotron resonant with H^+ band EMIC waves. In section 4, discussion and conclusions are presented.

2. Observations

Figure 1 shows an overview of the interplanetary magnetic field and solar wind plasma conditions on 22 June 2015, with 1-min resolution OMNI-2 data. An interplanetary shock (black dashed vertical line) arrived at the Earth's bow shock nose at 18:36 UT with interplanetary magnetic field Bz magnetic field turning southward, accompanied by a strong geomagnetic storm. The minimum SYM-H index reached −140 nT.

The Van Allen Probes mission, consisting of two nearly identical spacecraft (A and B), were launched into a highly elliptical, low inclination orbit with a perigee of about 600-km altitude, an apogee of 5.8 *Re* geocentric, and a period of 9 hr. The two Van Allen Probes are equipped with a variety of wave and particle instruments, which can be used to study radiation belt dynamics. On 22 June 2015, Van Allen Probe B was trailing Van Allen Probe A by 64 min with almost aligned locations, providing a good chance to investigate the time evolution of the radiation belt particle flux. Spin-averaged differential flux measured by the Relativistic Electron Proton Telescope (REPT) from the Energetic Particle, Composition, and Thermal Plasma Suite (Spence et al., 2013) data are adopted to study the time evolution of approximately megaelectron volt

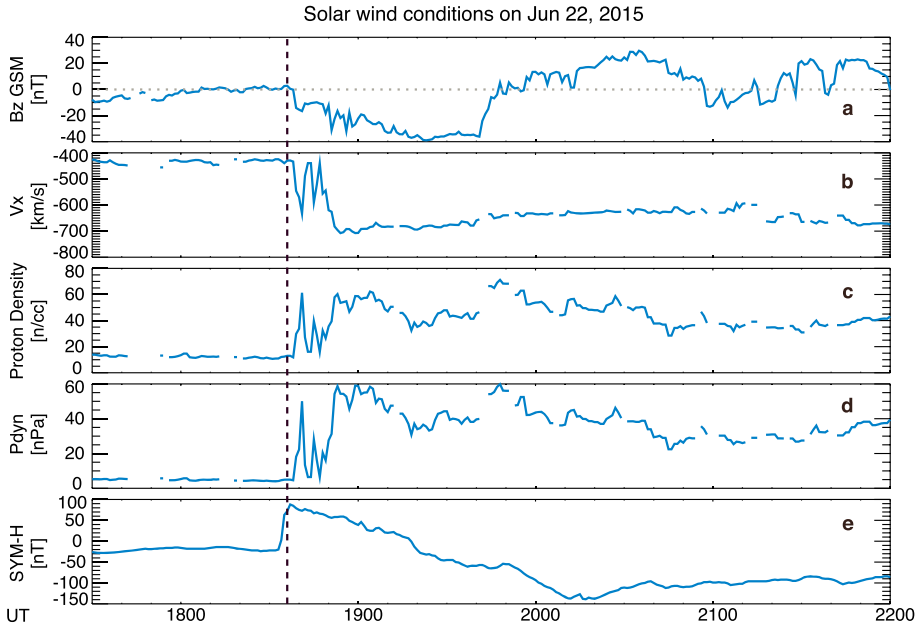

Figure 1. Solar wind magnetic field and plasma conditions on 22 June 2015, with 1-min resolution OMNI-2 data. (a) Z component of the interplanetary magnetic field in geocentric solar ecliptic coordinates. (b) X component of the solar wind velocity. (c) Proton density. (d) Solar wind dynamic pressure. (e) Geomagnetic activity SYM-H index. Black dashed vertical line represents the arrival of the shock.

electrons. Figure 2 shows measurements from Van Allen Probe A time shifted by 64 min to approximately align the L^* values of Van Allen Probe B. The flux decreased between passage of Van Allen Probe A and Van Allen Probe B. It can be seen that the flux dropout extends to higher L^* values at lower energies. The flux change in these low-energy channels (from 1.8 to 3.4 MeV) is greater outside $L^* \sim 4.5$. In the higher-energy channels (from 5.2 to 7.7 MeV), fluxes are depleted inside $L^* \sim 4$ and the observations are dominated by background at higher L^*. There could well have been depletion at larger L^* that would have been observed with lower background levels. The spatial location of this dropout at higher energies relative to the plasmapause is examined further below. The variation of 4.2-MeV electron fluxes shows characteristics in between the behavior described for low and high energies.

High-resolution (64 vectors per second) magnetic field data in geocentric solar magnetospheric coordinates from the fluxgate magnetometer in the Electric and Magnetic Field Instrument Suite and Integrated Science (EMFISIS) instrument on Van Allen Probe A and Van Allen Probe B (Kletzing et al., 2013) are utilized to investigate the EMIC waves. In order to obtain the wave power perpendicular to the ambient magnetic field, we transform the magnetic field vector from geocentric solar magnetospheric coordinates to field-aligned coordinates. EMIC wave power is thus obtained by applying the fast Fourier transform technique. Figures 3a and 3b show the EMIC wave power and wave normal angle observed by Van Allen Probe A. Both H^+ band and He^+ band EMIC waves are detected, with H^+ band EMIC waves occurring between L^* values of 1.9 to 3.2 at 19:28–21:10 UT, while He^+ band EMIC waves occur with L^* values of 1.9 to 2.7, beginning from 19:47 and ending at 21:10 UT. Figure 3b shows that the wave normal angles are below 10° relative to the background magnetic field, demonstrating that the EMIC waves are nearly parallel propagating. Figures 3c and 3d show the EMIC wave power and wave normal angle observed by Van Allen Probe B with −64-min time shift in order to approximately match the L^* values of Van Allen Probe A. Only low-amplitude H^+ band EMIC waves are observed. Figures 3e and 3f display the spin-averaged differential flux of the 5.2- and 6.3-MeV relativistic electrons observed by Van Allen Probe A (blue) and Van Allen Probe B (red, with −64-min time shift). Two red vertical dashed lines represent the two regions: (1) outside the plasmasphere. From 19:28:00 to 19:47:00 UT, H^+ band EMIC waves with stronger wave amplitude (0.1 nT^2/Hz) and electron fluxes observed by Van Allen Probe B are almost completely depleted. From 19:47:00 to 19:50:30 both H^+ band and He^+ band EMIC waves with weaker wave amplitude (0.05 nT^2/Hz) are observed, flux decreases but is not completely depleted; (2) inside the plasmasphere. After 19:50:30, both H^+ band and He^+ band EMIC waves with strong wave amplitude are observed and there is little change in flux. It is illustrated that (1) the dropout of 5.2-

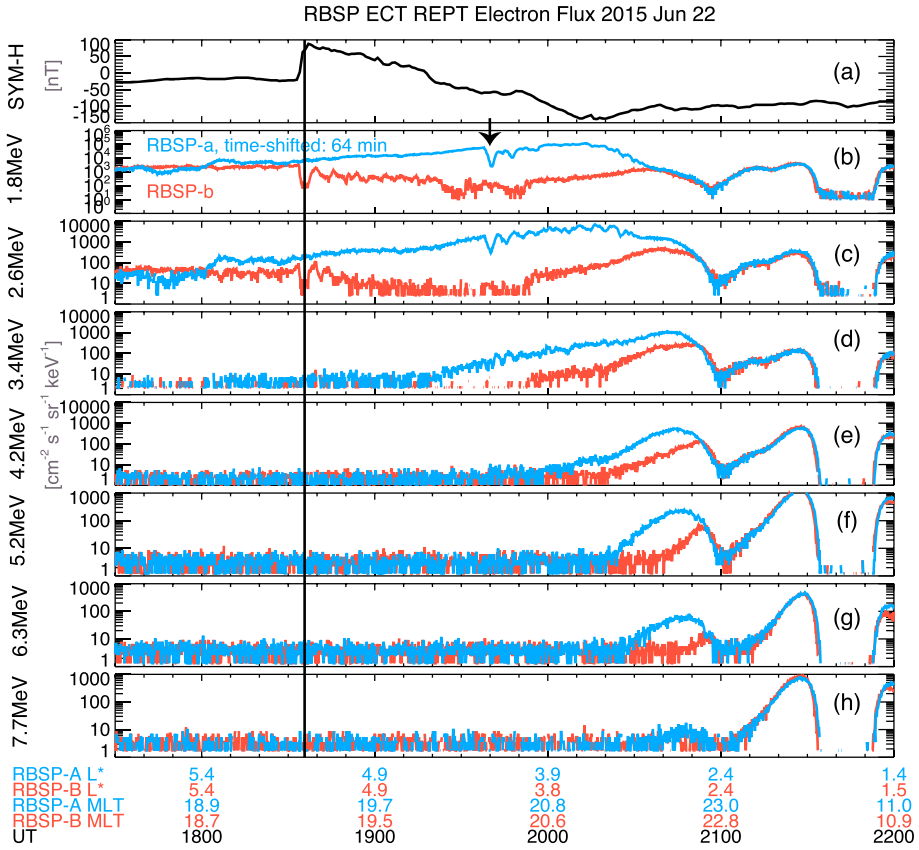

Figure 2. Overview of the electron flux loss during 1730 to 2200 UT. (a) SYM-H index indicates the shock arrival at 1836 UT. (b–h) Spin-averaged differential flux of the 1.8-, 2.6-, 3.4-, 4.2-, 5.2-, 6.3-, and 7.7-MeV electrons, measured by RBSP-A (blue) and RBSP-B (red). Note that in order to make the beginning of the dropout consistent with the time of shock arrival, RBSP-A measurements are shifted by 64 min to match the location of RBSP-B. Magnetic local time (MLT) and L for both satellites are labeled in the bottom. Vertical solid line indicates shock arrival at 18:36 UT (UT referred to Van Allen Probe B). Black arrow indicates shock arrival time at Van Allen Probe A. ECT = Energetic Particle, Composition, and Thermal Plasma Suite; REPT = Relativistic Electron Proton Telescope.

and 6.3-MeV relativistic electrons is coincident with the temporal and spatial region of the duskside H^+ band EMIC waves, indicating that the EMIC waves may account for depletion at low L^* values in Region 1. (2) Decrease in flux is smaller when the wave power is weaker at L^* values from 2.6 to 2.7 in Region 1. (3) Even though both H^+ band and He^+ band EMIC wave power is stronger (2 nT^2/Hz) in Region 2, the electron flux levels are unchanged between the Van Allen Probe A and Van Allen Probe B measurements. Note that Figure 2 is plotted by shifting spacecraft A with 64 min in order to make the beginning of the dropout consistent with the time of shock arrival, while Figure 3 is plotted by shifting spacecraft B with −64 min to show the real time of the waves since EMIC waves are mainly observed on spacecraft A.

Radial profiles of the spin-averaged differential flux of 5.2-MeV relativistic electrons within L^* values ranging from 2.5 to 3.6 for different orbits observed by Van Allen Probe A and Van Allen Probe B are shown in Figure 4. The dropout begins between 13:58 and 19:22 UT and ends before 20:27 UT. The shock arrives at 18:36 UT. The large change in flux observed by Van Allen Probe A inbound from 19:22 to 19:55 UT is likely produced by the Dst effect since PSD in this region does not change before 19:22 UT (Xiang et al., 2017). We focus analysis in the next section on the subsequent decrease in flux observed by Van Allen Probe B from 20:27 to 20:59 UT, 64 min later.

There are different mechanisms that can be responsible for the loss of relativistic electrons, each mechanism corresponding to a typical signature of pitch angle distribution after the loss. We examine the equatorial pitch angle distribution of RBSP-A (before the loss) and RBSP-B (after the loss), as shown in Figure 5. The equatorial magnetic field is calculated using the TS04 model, and the pitch angle distribution shown has been mapped to the equatorial plane. It can be seen that the REPT measurement only covers a narrow

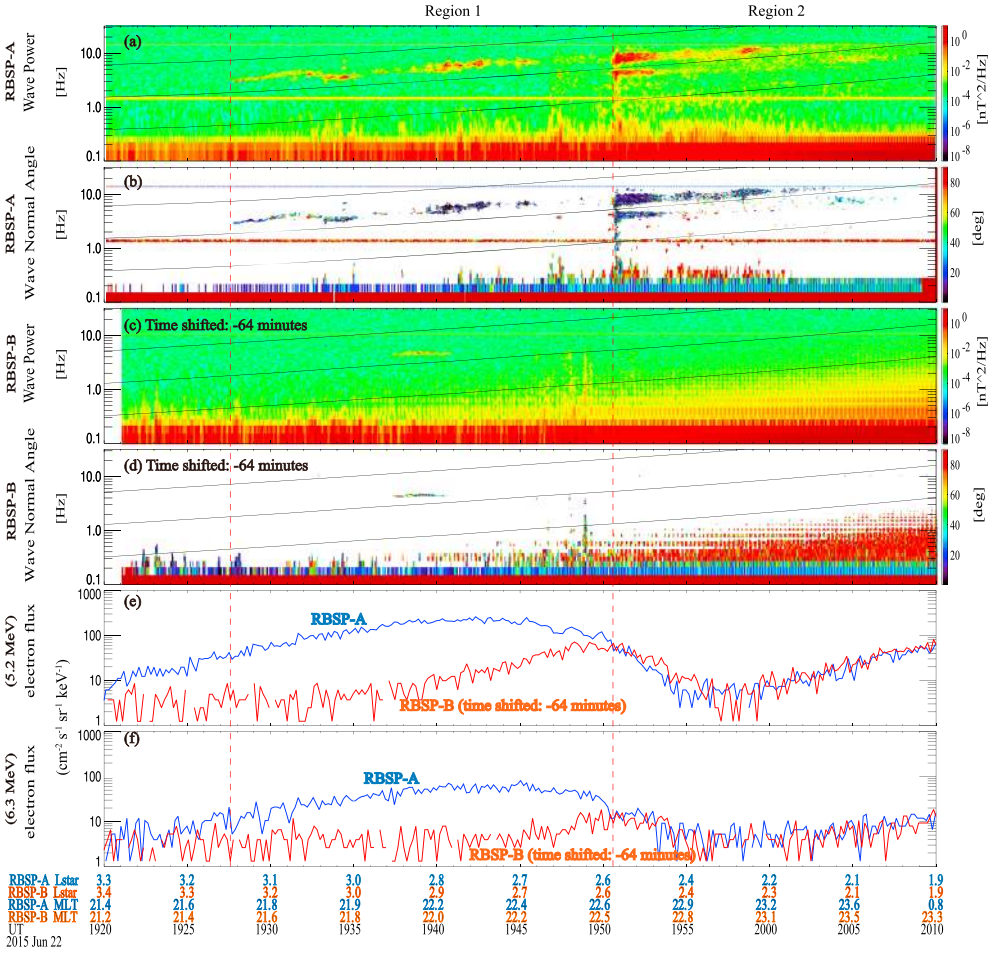

Figure 3. (a) Electromagnetic ion cyclotron (EMIC) wave power observed by Van Allen Probe A. (b) EMIC wave normal angle observed by Van Allen Probe A. (c) EMIC wave power observed by Van Allen Probe B with −64-min time shift. (d) EMIC wave normal angle observed by Van Allen Probe B with −64-min time shift. (e) Spin-averaged differential flux of the 5.2-MeV relativistic electrons observed by Van Allen Probe A (blue) and B (red, with −64-min time shift). (f) Spin-averaged differential flux of the 6.3-MeV relativistic electrons observed by Van Allen Probe A (blue) and B (red, with −64-min time shift). Superposed black lines in panels (a)–(d) refer to hydrogen (H^+), helium (He^+), and oxygen (O^+) ion gyrofrequencies. Two red vertical dashed lines represent the two intervals: (1) outside the plasmasphere between the two vertical lines and (2) inside the plasmasphere on the right of the second vertical line. Note that RBSP-B measurements are shifted by −64 min to match the location of RBSP-A. Magnetic local time (MLT) and L^* for both satellites are labeled at the bottom.

range of the equatorial pitch angles and it shows that the range of equatorial pitch angles over which flux decreases are seen includes [60,80]°. Thus, we cannot tell from the shape whether there is loss near 90° equatorial pitch angles or near the loss cone, which are not measured at the times shown due to spacecraft inclination. In the next section, five different mechanisms will be considered and discussed to explain the loss of >5.2-MeV electrons.

3. Loss Mechanisms

3.1. Radial Loss to the Magnetopause

In Figure 3, we show that the high-energy losses in 5.2- and 6.3-MeV REPT channels occur mainly within $L^* = 3.4$, below the last closed drift shell at $L^* = 3.7$ (Xiang et al., 2017). Thus, it is hard to explain the high-energy loss deep inside the magnetosphere as due to magnetopause shadowing. Subsequent outward radial diffusion is another potential explanation, but it can take days for the electrons to diffuse 1 *Re* outward from such low L^* (Ali et al., 2016; Brautigam & Albert, 2000; Li et al., 2016, 2017, Ozeke & Mann, 2004). For this event, radial diffusion coefficients have a magnitude of 10^{-2} day^{-1} during the loss of high-energy electrons (not shown). This process is too slow to account for the rapid loss within 64 min. Thus, at higher

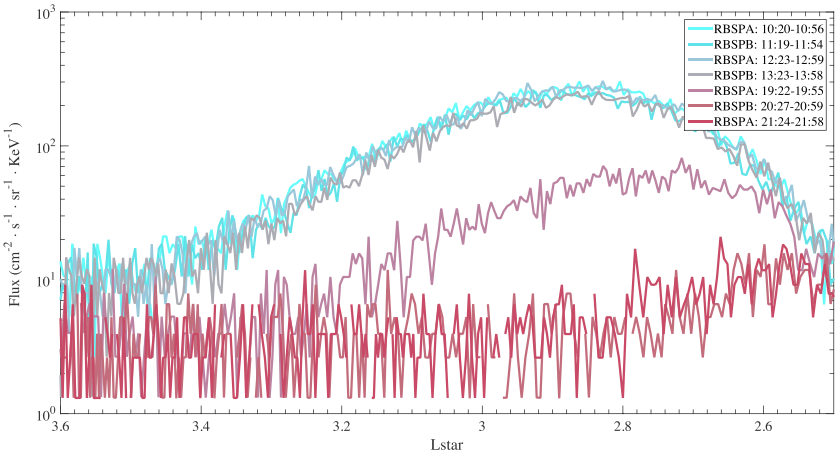

Figure 4. Radial profiles of the spin-averaged differential flux of 5.2-MeV electrons, with different colors referring to different satellite orbits.

L^* values and lower energies, radial loss to the magnetopause is a viable explanation (Xiang et al., 2017), whereas the loss at low L^* values for higher-energy electrons cannot be produced by radial loss to the magnetopause.

3.2. Pitch Angle Scattering by Whistler Mode Waves

Whistler mode chorus and hiss emissions are two intensely occurring electromagnetic waves in the Earth's magnetosphere and have been shown to play an important role in precipitating electrons into the atmosphere (Ozeke et al., 2004; Summers et al., 2007). Whistler mode chorus waves are often observed outside the plasmasphere and thus could be responsible for the loss of relativistic electrons in Region 1. Satellite measurements can only provide information at a particular radial distance and MLT. We have no measurements from Van Allen Probes for the dawn sector for this event where very low frequency (VLF) chorus waves tend to occur (Meredith et al., 2003, 2012). Chorus wave activity can also be inferred from low-altitude electron measurements by POES (Li et al., 2013), but 22 June 2015 is also a solar proton event; therefore,

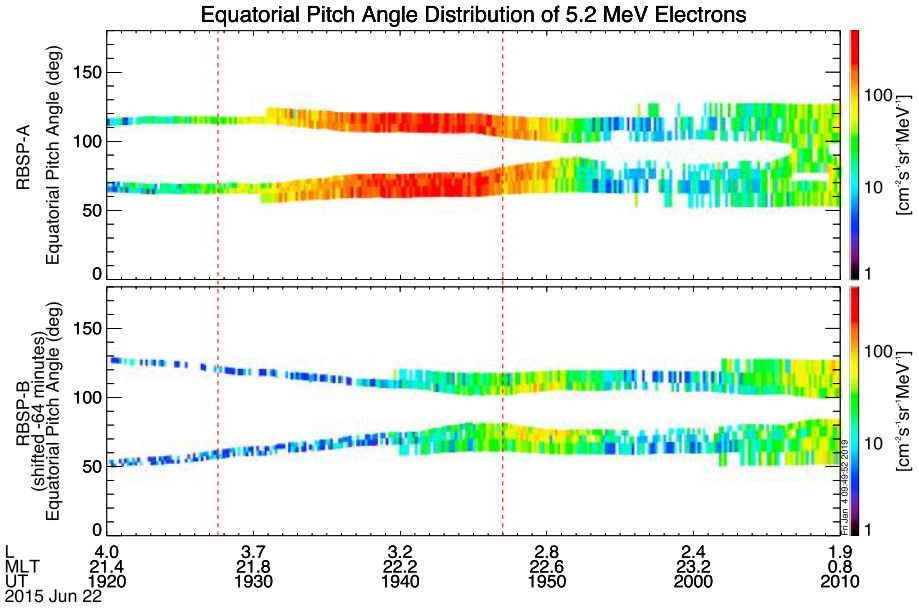

Figure 5. (a) Equatorial pitch angle distribution of 5.2-MeV relativistic electrons measured by Van Allen Probe A. (b) Equatorial pitch angle distribution of 5.2-MeV relativistic electrons measured by Van Allen Probe B, shifted by −64 min to match the location of Van Allen Probe A. Region between two red dashed lines represents where loss is observed outside the plasmasphere.

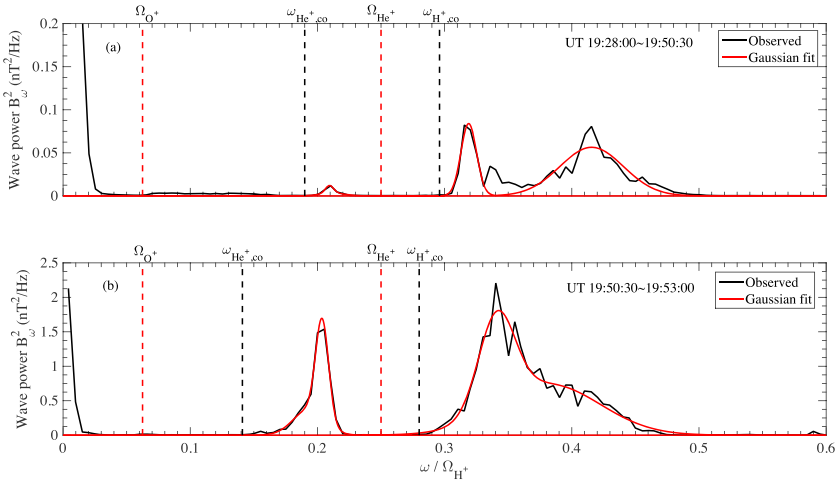

Figure 6. Time-averaged magnetic field wave power spectra in (a) Region 1 and (b) Region 2. Red vertical dashed lines are He^+ and O^+ gyrofrequencies. Black vertical dashed lines are cutoff frequencies for H^+ band ($\omega_{H^+,co}$) and He^+ band ($\omega_{He^+,co}$). The normalized H^+ cyclotron frequency is 1 and is off the scale to the right.

the electron energy channels are contaminated by the solar protons. Hiss waves primarily occur inside the plasmasphere and dayside drainage plumes. At other MLT, hiss waves can also be a potential cause of loss since the plasmapause is asymmetric and moves back and forth during such disturbed conditions. However, for such high-energy electrons, pitch angle scattering by whistler mode waves is much slower than the 1-hr time scale of observed loss (Thorne et al., 2013).

3.3. Bounce Resonance With H^+ Band EMIC Waves

H^+ band EMIC waves are able to resonate with electrons over a wide range of L shells and energies through a bounce resonance mechanism (Cao et al., 2017). Bounce-resonant electron pitch angle scattering rates show a strong dependence on L shell. Both decreasing the L shell and increasing density result in weaker rates of pitch angle scattering. At $L = 3$, pitch angle scattering occurs in a limited range near 90°. In our case study, the electron loss and EMIC wave activity in Region 1 corresponds to relatively high density and low L shell, as determined in the next section from the upper hybrid resonance (UHR); thus, the loss rate is low for scattering relativistic electrons with equatorial pitch angle of [60°,80°]. Estimates of the loss time scale for $L = 3.5$ and density of 317 cm^{-3} based on Cao et al. (2017) are of the orders of 10 days. Thus, bounce resonance by itself cannot explain the observed loss in 64 min.

3.4. Cyclotron Resonance With H^+ Band EMIC Waves

3.4.1. Wave Properties and Plasma Parameters

In order to test whether EMIC waves can scatter relativistic electrons through cyclotron interaction into the loss cone on the time scale between passage of the A and B spacecraft in Figures 2–4 (lower curves), we first calculate the minimum energy (E_{min}) for electrons to resonate with parallel propagating EMIC waves and the diffusion coefficient for EMIC waves to precipitate electrons in a multi-ion (H^+, He^+, and O^+) species plasma.

The minimum resonant energy, which depends on the plasma parameter $\alpha^* = {\Omega_e}^2/{\omega_{pe}}^2$, the background cold ion composition and the propagation band of the EMIC waves, is calculated using methods in Summers and Thorne (2003), where $\Omega_e = eB/m_e$ is the electron gyrofrequency and $\omega_{pe}^2 = n_0 e^2/\epsilon_0 m_e$ is the plasma frequency squared, e is the electron charge, m_e is the mass of electrons, B is the background magnetic field, ϵ_0 is vacuum permittivity, and n_0 is the electron density. The minimum resonant energy increases as the value of α^* increases.

EMIC waves cannot propagate when the wave number k becomes imaginary. Cutoff frequencies are defined where the wave number vanishes. If H^+ band and He^+ band EMIC waves are observed simultaneously, cold ion composition can be obtained from the cutoff frequencies of the two stop bands (Min et al., 2015). In our case, H^+ band and He^+ band EMIC waves are observed simultaneously from 19:47:00 to 19:50:30 UT in Region 1 and from 19:50:30 to 19:53:00 UT in Region 2 in Figure 3. Time-averaged magnetic field wave power spectra are plotted in Figure 6 for the two different regions in Figure 3. The superposition of two Gaussian

Table 1
Gaussian Fit Parameters for Each Band in Each Region

Gaussian fit parameters	Region 1 (H^+ band)	Region 1 (He^+ band)	Region 2 (H^+ band)	Region 2 (He^+ band)
Center frequency (ω_{m1}/Ω_{H^+})	0.319	0.209	0.340	0.203
Center frequency (ω_{m2}/Ω_{H^+})	0.417	0.212	0.381	0.193
Half band width($\delta\omega_1/\Omega_{H^+}$)	0.009	0.005	0.020	0.007
Half band width($\delta\omega_2/\Omega_{H^+}$)	0.04	0.0140	0.057	0.017
$(\omega_{m2}+3*\delta\omega_2)/\Omega_{H^+}$	0.522	0.257	0.554	0.246
$(\omega_{m2}-3*\delta\omega_2)/\Omega_{H^+}$	0.310	0.170	0.210	0.141
$(\omega_{m1}+3*\delta\omega_1)/\Omega_{H^+}$	0.345	0.223	0.401	0.225
$(\omega_{m1}-3*\delta\omega_1)/\Omega_{H^+}$	0.293	0.196	0.280	0.182
Upper-frequency limit ($/\Omega_{H^+}$)	0.522	0.223	0.520	0.225
Lower-frequency limit ($/\Omega_{H^+}$)	0.293	0.196	0.280	0.141

shapes, of the form $a1 * e^{-(\omega-\omega_{m1})^2/2\delta\omega_1^2} + a2 * e^{-(\omega-\omega_{m2})^2/2\delta\omega_2^2}$, is applied to fit the observed wave power spectrum for each band in each region. The parameters of two-term Gaussian models of each band in each region are shown in Table 1. It can be seen that the lower-frequency limits ($\omega_{m1}-3*\delta\omega_1$) are approximately consistent with the observed cutoff frequencies in each band in the last line. The cutoff frequencies for H^+ band ($\omega_{H^+,co}$) and He^+ band ($\omega_{He^+,co}$) are 0.293 Ω_{H^+} and 0.196 Ω_{H^+}, respectively, in units of the hydrogen gyrofrequency in Region 1. In Region 2, the cutoff frequencies are 0.280 Ω_{H^+} and 0.141 Ω_{H^+} for H^+ band and He^+ band EMIC waves, respectively. Using the formulas in Min et al. (2015), we can obtain the cold ion compositions, with percentages $\eta_{H^+} = 80.84\%$, $\eta_{He^+} = 1.65\%$, and $\eta_{O^+} = 17.51\%$ in Region 1 and $\eta_{H^+} = 87.96\%$, $\eta_{He^+} = 2.33\%$, and $\eta_{O^+} = 9.71\%$ in Region 2.

The wave amplitude and plasma density are shown in Figure 7. Figure 7a shows the wave amplitude calculated for frequency between 2 and 20 Hz in each region. Figure 7b shows the plasma density obtained from the EMFISIS UHR frequency from Van Allen Probe A. The red dashed vertical lines refer to the same universal time as the second dashed vertical lines in Figure 3. From the density plot (Figure 7b), it can be seen that Region 1 is outside the plasmasphere and Region 2 is inside the plasmasphere (drop in plasma density of a factor of 0.8 within $L = 0.1$ at the boundary of Region 1 and Region 2). The density begins to rise after 19:37 UT toward the value of ~3,000 cm^{-3} in Region 2.

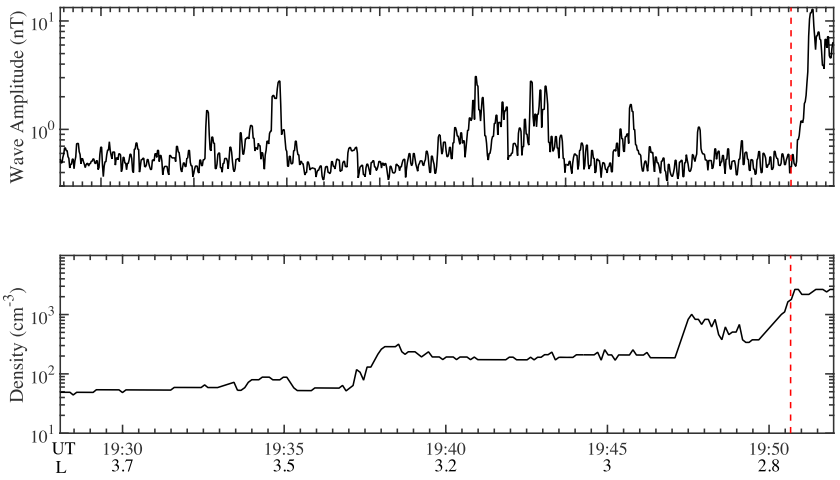

Figure 7. (a) The wave amplitude calculated for frequency between 2 and 20 Hz in different regions. (b) The plasma density obtained from the upper hybrid resonance frequency. The red dashed vertical line refers to the same universal time as the second dashed vertical lines in Figure 3. Measurements are taken from Van Allen Probe A.

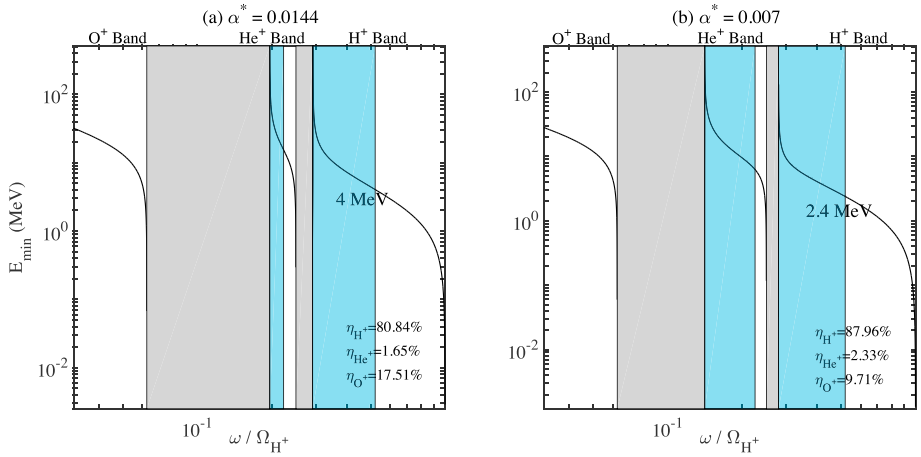

Figure 8. Minimum resonant energy as a function of frequency in (a) Region 1 and (b) Region 2 . The light gray areas are the two stop bands, and light blue areas are the observed propagation bands. The numbers 4 and 2.4 MeV indicate the minimum energy for H^+ band electromagnetic ion cyclotron waves to interact with electrons at the upper frequency limit.

3.4.2. Minimum Resonant Energy

Substituting the minimum value of α^* (0.0144 in Region 1 and 0.007 in Region 2) and cold ion compositions in each region, the minimum resonant energy is shown in Figure 8. The light gray areas are the two stop bands, and light blue regions are the observed propagation bands according to Figure 6. The minimum energies for electrons to resonate with H^+ band EMIC waves are as follows: (1) In Region 1 where the loss is observed, E_{min} is about 4 MeV at a frequency of about 0.52 Ω_H^+, which is below the observed loss at 5.2 MeV outside the plasmasphere of Figure 3. The minimum energy for electrons to resonate with He^+ band EMIC waves in Region 1 is about 15 MeV, which is higher than observation. We can conclude that it is the H^+ band EMIC waves rather than the weak He^+ band EMIC waves outside the plasmasphere that may account for the rapid loss of >5.2-MeV relativistic electrons if due to cyclotron resonance. (2) In Region 2, the minimum energy for electrons to resonate with H^+ band EMIC waves is about 2.4 MeV; however, loss is not observed in Region 2 of Figure 3, as discussed further below.

3.4.3. Pitch Angle Diffusion Coefficient

In order to test whether the loss time scale of relativistic electrons driven by H^+ band EMIC waves is consistent with the observed loss rate, a bounce-averaged pitch angle diffusion coefficient has been calculated using methods in Summers et al. (2007). Averaged wave amplitude is chosen to be 2 and 7 nT in Region

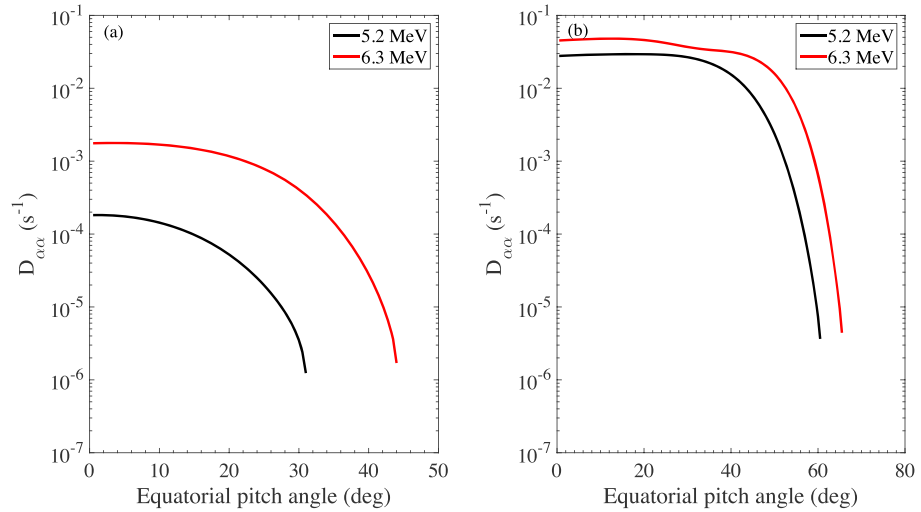

Figure 9. Pitch angle diffusion coefficient of H^+ band electromagnetic ion cyclotron waves (a) outside and (b) inside the plasmapause. The kink in the red line in panel (b) is due to the double Gaussian spectrum inferred from Figure 6.

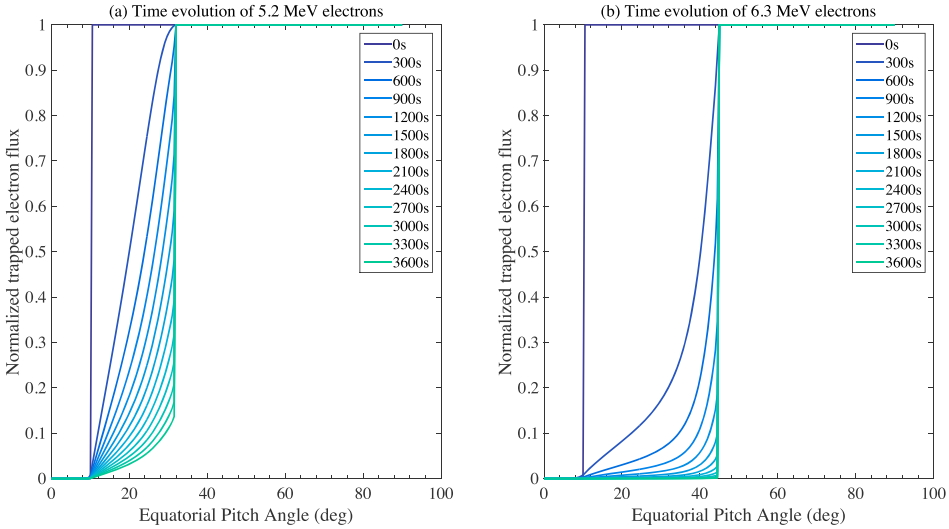

Figure 10. (a) Time evolution of 5.2-MeV trapped electron fluxes in Region 1. (b) Time evolution of 6.3-MeV trapped electron fluxes in Region 1. Different colors represent electron flux at different simulation times.

1 and Region 2 from Figure 7a, respectively, and as the latitudinal extent is narrow, $\delta B/B_o$ is kept constant with latitude. Gaussian fit parameters shown in Table 1 are adopted to calculate the EMIC wave diffusion coefficients. All the other parameters are chosen at 19:38:30 and 19:50:40 UT in Region 1 and Region 2, respectively. The local magnetic field B_o is 833 and 1,404 nT measured by the fluxgate magnetometer of the EMFISIS instrument on board Van Allen Probes, corresponding to 731 and 1,233 nT at the equator. Background electron number densities are 317 and 1,801 cm^{-3} obtained from the EMFISIS UHR frequency, respectively, in the two regions. Latitudinal coverage of EMIC waves to interact with relativistic electrons is confined to ±15° at the equator (Li et al., 2014), and drift coverage is chosen to be 15% of the total electron drift orbit, assuming that the EMIC waves have broad spatial azimuthal scale (Clausen et al., 2011). The magnitude of the diffusion coefficient scales linearly with the fraction of drift orbit assumed. The pitch angle diffusion coefficients for 5.2- and 6.3-MeV electrons are plotted in Figure 9a outside the plasmasphere and Figure 9b inside the plasmapause. Simulated time evolution of the trapped 5.2- and 6.3-MeV electron flux in Region 1 is shown in Figure 10 by solving the bounce-averaged diffusion equation (Li et al., 2014). An equatorial loss cone of 10° is calculated assuming a dipole magnetic field model. The REPT instrument only

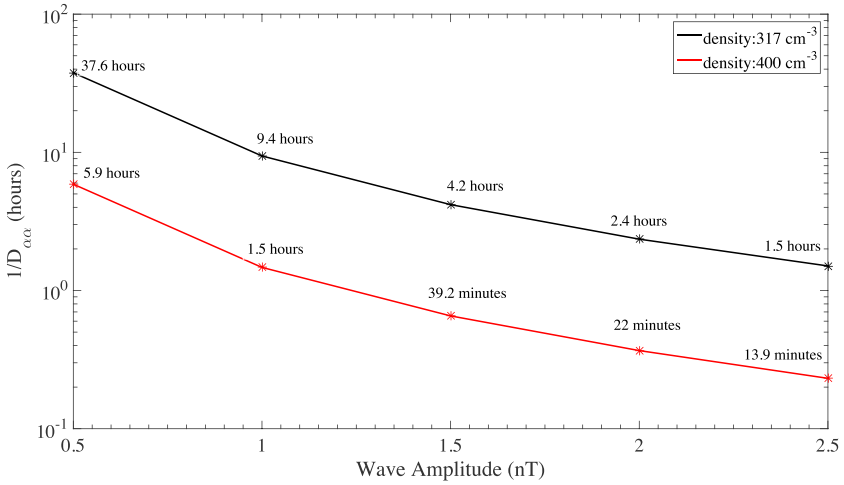

Figure 11. Minimum pitch angle diffusion time scale for electrons at small pitch angles of H^+ band electromagnetic ion cyclotron waves outside the plasmasphere for different density and wave amplitude assumptions. Black is the diffusion time scale with density of 317 cm^{-3}, and red is with density of 400 cm^{-3}. Other parameters stay the same as in Figure 9a.

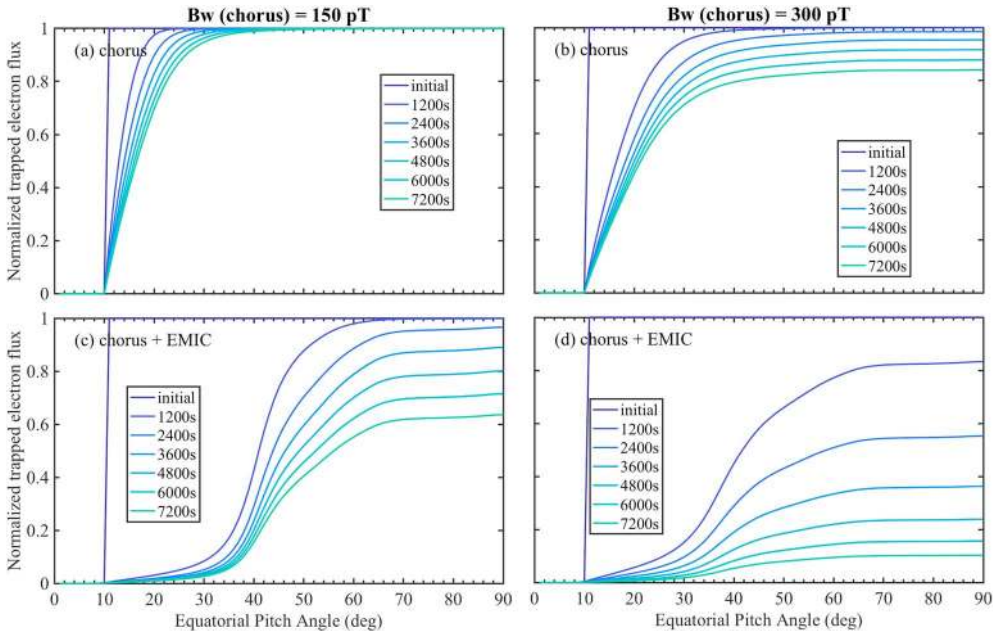

Figure 12. Time evolution of 5.2-MeV trapped electron fluxes when interacting with (a) 150-pT chorus waves only, (b) 300-pT chorus waves only, (c) electromagnetic ion cyclotron (EMIC) waves and 150-pT chorus waves, and (d) EMIC waves and 300-pT chorus waves. Different colors represent normalized electron flux at different simulation times. For EMIC waves, background electron number density is 400 cm^{-3}. Other parameters stay the same as Figure 10. For chorus waves, background electron number density is 1 cm^{-3}.

covers a narrow range of the equatorial pitch angles after the shock arrival; thus, the complete initial pitch angle distribution is not available. Here, an isotropic flux is assumed outside the loss cone. It can be seen from Figure 10a that most of the electrons are depleted in 1-hr time scale where diffusion coefficients are greater than 0 and thus may explain the rapid loss of the trapped relativistic electrons at small pitch angles.

The cyclotron resonant diffusion coefficient depends strongly on the wave amplitude and background number density in Region 1 and Region 2. We investigated different wave amplitudes and background number densities, keeping other conditions the same as in Figure 9a to calculate the minimum loss time scale for electrons at small pitch angles as the inverse of the maximum pitch angle diffusion coefficient. The results are shown in Figure 11, demonstrating that the diffusion time scale decreases when wave amplitude and density increase. When the number density increases from 317 to 400 cm^{-3}, the minimum loss time scale is 12 times lower than that for number density of 317 cm^{-3}. Note that the loss ratio in the 5.2-MeV energy channel at 19:38 UT is about 95%, corresponding to an *e*-folding time of 21 min when electron flux drops by 1/e. When wave amplitude reaches 2 nT and number density is 400 cm^{-3}, the minimum loss time scale is 22 min, comparable to the observed 21 min.

3.5. Combined Effects of H^+ Band EMIC Waves and Whistler Mode Chorus Waves

Even if EMIC waves do not resonate with electrons within observed [60°,80°] pitch angles, they create strong gradients in pitch angle, as shown in Figure 10. Pitch angle transport is diffusive, and the net diffusive flux is proportional not only to the diffusion coefficient but also to the gradient. The gradients that result from bite outs at small pitch angles through cyclotron interaction with EMIC waves increase the diffusion rate due to other mechanisms acting at higher pitch angles. Shprits et al. (2016) have shown that 4.2-MeV electrons diffuse rapidly at all pitch angles when VLF waves (e.g., chorus outside the plasmasphere, hiss inside, or hiss in plumes) and EMIC waves are combined in their diffusive effect along an electron drift path, and only when EMIC waves are included, see their Figure 4. There is always some VLF wave activity, which is enhanced during storms (Meredith et al., 2003, 2004, 2012). Electrons encounter scattering by these waves at higher pitch angles, which feed EMIC scattering that is very efficient at low pitch angles, transporting electrons into the loss cone.

Figure 12 shows the time evolution of 5.2-MeV trapped electron fluxes when interacting with chorus waves only (Figures 12a and 12b) and with combined effects of EMIC and chorus waves (Figures 12c and 12d).

Figure 10 demonstrates that [60°, 80°] near equatorial pitch angle electrons are not influenced by EMIC waves. Panels Figures 12a and 12b show that chorus waves solo can only deplete less than 20% of electrons with [60°, 80°] near equatorial pitch angles in 2 hr. But when we combined EMIC waves and 300-pT chorus waves together, over 90% of electrons are depleted in 2 hr. It can be concluded that chorus waves with large wave amplitude can provide a reasonable loss rate for 5.2-MeV electrons when combined with the observed EMIC waves on 22 June 2015. Chorus wave amplitude increases with geomagnetic activity (Li et al., 2009) and large-amplitude whistler mode waves (>80 pT) are often observed during active periods ($AE > 200$ nT; Wilson et al., 2011). The 240-mV/m (800-pT) chorus waves have been observed when the *AE* index reached a peak value of 800 nT by Cattell et al. (2008). On 22 June 2015, the *AE* index reached 2,000 nT, so it is reasonable to expect that the wave amplitude could have been greater than 300 pT during this large storm. This calculation is illustrative of possible effects of EMIC waves in conjunction with chorus in causing precipitation of the ultrarelativistic electron population.

4. Discussion and Conclusions

In this study, rapid loss of ≥5.2-MeV radiation belt electrons is investigated associated with local H^+ band EMIC waves at unusually low L^* values (2.4–3.2) outside the plasmasphere during an extreme magnetopause compression event, with five mechanisms considered.

The flux dropout in low- and high-energy channels shows different behaviors in Figure 2, suggesting different loss mechanisms. Xiang et al. (2017) investigated this event and explained the electron flux drop with energy below 5.2 MeV with magnetopause shadowing. REPT observations show that the high-energy losses in 5.2- and 6.3-MeV REPT channels occur mainly within $L^* = 3.4$, below the last closed drift shell at $L^* = 3.7$ (Xiang et al., 2017). Thus, it is difficult to explain the high-energy loss deep inside the magnetosphere as due to magnetopause shadowing. Subsequent outward radial diffusion is another potential explanation but it can take days for the electrons to diffuse 1 *Re* outward from such low L^* (Ali et al., 2016; Brautigam & Albert, 2000; Li et al., 2016, 2017; Ozeke & Mann, 2004). For this event, radial diffusion coefficients have a magnitude of 10^{-2} day^{-1} during the loss of high-energy electrons (not shown). This process is too slow to account for the rapid loss within 64 min. Thus, at higher L^* values and lower energies, radial loss to the magnetopause is a viable explanation, whereas at low L^* values for higher-energy electrons, the loss may be driven by EMIC waves at low pitch angles. At higher pitch angles, given strong gradients in pitch angle due to fast EMIC wave diffusion evident in Figure 10, diffusion due to VLF waves may be even more efficient than absent the EMIC wave scattering at low pitch angles (Shprits et al., 2016).

It was demonstrated that EMIC waves can cause electron loss at low pitch angles and no loss at near equatorial pitch angles (Usanova et al., 2014). In this particular case, however, neither measurement of pitch angle distribution at low pitch angles nor near 90° pitch angles is available due to spacecraft inclination and morphology of the background magnetic field during the strong geomagnetic storm studied (Xiang et al., 2017). In order to further investigate for the causal connection between EMIC waves and loss of relativistic electrons and to examine the factors that influence the capability of EMIC waves in precipitating relativistic electrons, minimum resonant energy and pitch angle diffusion coefficients for electrons to interact with EMIC waves have been calculated. Cold ion composition, which has a strong influence on both the minimum resonant energy and diffusion coefficient (Summers & Thorne, 2003; Uzbekov et al., 2016), is usually adopted with typical values (Su et al., 2017) when investigating EMIC-driven pitch angle scattering of relativistic electrons. Substituting the typical values $\eta_{H^+} = 70\%$, $\eta_{He^+} = 20\%$, and $\eta_{O^+} = 10\%$ (Meredith et al., 2003; Summers & Thorne, 2003), only waves with frequency above 0.45 Ω^+_H can resonate with relativistic electrons outside the plasmasphere. The minimum resonant energy would be 6.58 MeV and quickly goes up to 48 MeV at 0.45 Ω^+_H where there is measurable wave power for the event studied (not shown), much higher than the energy of electrons with observed flux dropout at low *L* values. However, studies have shown that the heavy ion concentration varies with geomagnetic activity and different regions in the magnetosphere (Denton et al., 2014). Since direct measurement of low energy ions is affected by the spacecraft potential (Spence et al., 2013), here we adopted the method in Min et al. (2015), using the cutoff frequencies of the two stop bands of EMIC waves to calculate the cold ion composition. As can be clearly seen in Figure 6, the uncertainty of the cutoff point is within 0.02 ω/Ω_{H^+}. Deviations in cold ion composition determined by this method are less than 1% when the cutoff frequency of H^+ band and He^+ band determined from the wave spectrum is within an error of 0.02 ω/Ω_{H^+}. The H^+, He^+, and O^+ ions constitute 80.84%, 1.65%, and 17.51% of the total cold plasma ions in Region 1 and 84.82%, 1.78%, and 12.62% in Region 2. Compared to the

typically used cold ion compositions, He^+ composition is less and O^+ composition is enriched. This is consistent with a heavy ion concentration study showing that O^+ ions are rich in the plasma trough (Takahashi et al., 2008) and during storm times (Hamilton et al., 1988; Korth et al., 2002). These improved estimates for ion composition lower the minimum resonant energies for electrons to resonate with H^+ band EMIC waves outside the plasmasphere to 4 MeV. Thus, resonance with EMIC waves may explain the observed loss at 5.2 MeV at small pitch angles. E_{min} for the He^+ band EMIC waves to interact with relativistic electrons is about 15 MeV, which is higher than observations of precipitation.

The electron flux is almost completely depleted outside the plasmasphere during the 64 min between passage of the A and B spacecraft after the shock arrival at 18:36 UT. The loss ratio in the 5.2-MeV energy channel during a period between 19:38 UT (RBSP-A passage) and 20:42 UT (RBSP-B passage) is about 95%, corresponding to an *e*-folding time of 21 min when electron flux drops by 1/e. Theoretical diffusion time scale for different electron number density and wave amplitude is also evaluated at 19:38, as shown in Figure 11. When wave amplitude reaches 2 nT and number density is 400 cm^{-3}, the diffusion time scale is 22 min, comparable to an observed *e*-folding time of 21 min. Such a small increase in both the observed plasma number density and wave amplitude is highly plausible during the loss. First, the location of the plasmapause is highly dynamic during this period. Part of Region 1 is very likely inside the plasmapause as the RBSP-A spacecraft moves earthward during the shock orbit and the plasmapause only becomes so strongly compressed as measured by the A spacecraft when it moves into Region 2, but certainly not before or even immediately after the shock arrives. Second, recent geomagnetic activity will add to the uncertainties of the electron density determined from the UHR frequency, especially in the plasma trough (Kurth et al., 2015). Third, the wave amplitude varies during this period and the average amplitude may exceed 2 nT during this period. Given the uncertainties in plasma density as well as wave amplitude, Figure 11 shows that the electron loss time scale due to H^+ band EMIC waves is consistent with the observed loss time scale inferred from Figure 3.

Quasi-linear diffusion by EMIC waves alone cannot lead to strong and fast dropout of megaelectron volt electrons up to high pitch angles and the diffusion rate is low compared to the observed loss time when interacting with chorus waves alone. But the combined effect of EMIC waves and whistler mode waves can effectively deplete such energetic electrons extending to high pitch angles (Li et al., 2007; Ma et al., 2015; Mourenas et al., 2016; Shprits et al., 2016; Zhang et al., 2017). In this particular case, chorus waves with large wave amplitude (>300 pT) can cause rapid loss of 5.2 MeV when combined with the observed EMIC waves on 22 June 2015. Other mechanisms such as bounce resonance with H^+ EMIC waves near 90° pitch angle may contribute to this process of diffusing electrons toward lower pitch angles.

In Region 2, although the minimum resonant energy is lower and the diffusion coefficient is higher than outside the plasmasphere, the flux has almost no change. Whistler mode chorus that may contribute to pitch angle diffusion at higher pitch angles in concert with EMIC waves is replaced by hiss inside the plasmasphere as the dominant VLF wave mode responsible for pith angle scattering with a longer loss time scale (Orlova et al., 2016). Thus, diffusion at higher pitch angles toward lower ones where EMIC wave diffusion is strong may be less effective inside the plasmapause. Additionally, the maximum wave amplitude is about 12 nT, reaching the strong diffusion limit, where quasi-linear theory may no longer apply. Phase bunching without trapping, the commonly expected nonlinear behavior, may lead to advection toward large pitch angles, rather than diffusion toward the loss cone (Albert & Bortnik, 2009). Thus, the observed small flux change in Region 2 might be modified by nonlinear effects.

From above, we can conclude that VLF wave activity that is enhanced during storms may combine with cyclotron interaction with H^+ band EMIC waves to cause the rapid loss of the relativistic electrons on the 1-hr time scale between passage of the twin Van Allen Probe spacecraft through the outer zone into the plasmasphere following arrival of the interplanetary shock at 18:36 UT on 22 June 2015. There is lack of VLF wave observations in the postnight to noon local time sector for this event, with Van Allen Probes premidnight and a solar proton event contaminating POES electron precipitation measurements, which have been used as a proxy for chorus (Li et al., 2013). However, the strong observational correlation between >5.2-MeV electron loss at low L^* and H^+ band EMIC waves observed outside the plasmapause suggest that the latter play a critical role in diffusing electrons into the loss cone on the 1-hr time scale of satellite separation for the 22 June 2015 electron dropout event.

Acknowledgments
This work was supported by NASA Grant NNX15AF54G and JHU/APL under NASA contracts NNN16AA09T and NNN06AA01C to UMN and UNH with subcontracts to Dartmouth. We would like to thank David Malaspina for discussion of Van Allen Probes EFW spacecraft potential measurement of density, Maulik Patel for discussion of MHD test particle simulations of the 22 June 2015 storm, and also Richard Denton and Maria Usanova for discussing the EMIC loss mechanism. The Van Allen Probe EMFISIS data can be obtained at the EMFISIS website (https://emfisis.physics.uiowa.edu/data/index), and REPT data can be downloaded from the RBSP website (https://www.rbsp-ect.lanl.gov/science/DataDirectories.php).

References

Albert, J. M., & Bortnik, J. (2009). Nonlinear interaction of radiation belt electrons with electromagnetic ion cyclotron waves. *Geophysical Research Letters*, *36*, l12110. https://doi.org/10.1029/2009GL038904

Ali, A. F., Malaspina, D. M., Elkington, S. R., Jaynes, A. N., Chan, A. A., Wygant, J., & Kletzing, C. A. (2016). Electric and magnetic radial diffusion coefficients using the Van Allen Probes data. *Journal of Geophysical Research: Space Physics*, *121*, 9586–9607. https://doi.org/10.1002/2016JA023002

Brautigam, D. H., & Albert, J. M. (2000). Radial diffusion analysis of outer radiation belt electrons during the October 9, 1990, magnetic storm. *Journal of Geophysical Research*, *105*(A1), 291–309. https://doi.org/10.1029/1999JA900344

Cao, X., Ni, B., Summers, D., Bortnik, J., Tao, X., Shprits, Y. Y., et al. (2017). Bounce resonance scattering of radiation belt electrons by H^+ band EMIC waves. *Journal of Geophysical Research: Space Physics*, *122*, 1702–1713. https://doi.org/10.1002/2016JA023607

Capannolo, L., Li, W., Ma, Q., Shen, X.-C., Zhang, X.-J., Redmon, R. J., Rodriguez, J. V., Engebretson, M. J., Kletzing, C. A., Kurth, W. S., Hospodarsky, G. B., Spence, H. E., Reeves, G. D., & Raita, T. (2019). Energetic electron precipitation: Multievent analysis of its spatial extent during EMIC wave activity. *Journal of Geophysical Research: Space Physics*, *124*. https://doi.org/10.1029/2018JA026291

Capannolo, L., Li, W., Ma, Q., Zhang, X.-J., Redmon, R. J., Rodriguez, J. V., et al. (2018). Understanding the driver of energetic electron precipitation using coordinated multisatellite measurements. *Geophysical Research Letters*, *45*, 6755–6765. https://doi.org/10.1029/2018GL078604

Cattell, C., Wygant, J. R., Goetz, K., Kersten, K., Kellogg, P. J., von Rosenvinge, T., et al. (2008). Discovery of very large amplitude whistler-mode waves in Earth's radiation belts. *Geophysical Research Letters*, *35*, L01105. https://doi.org/10.1029/2007GL032009

Clausen, L. B. N., Baker, J. B. H., Ruohoniemi, J. M., & Singer, H. J. (2011). EMIC waves observed at geosynchronous orbit during solar minimum: Statistics and excitation. *Journal of Geophysical Research*, *116*(A10205). https://doi.org/10.1029/2011JA016823

Denton, R. E., Jordanova, V. K., & Fraser, B. J. (2014). Effect of spatial density variation and O^+ concentration on the growth and evolution of electromagnetic ion cyclotron waves. *Journal of Geophysical Research: Space Physics*, *119*, 8372–8395. https://doi.org/10.1002/2014JA020384

Drozdov, A. Y., Shprits, Y. Y., Usanova, M. E., Aseev, N. A., Kellerman, A. C., & Zhu, H. (2017). EMIC wave parameterization in the long-term VERB code simulation. *Journal of Geophysical Research: Space Physics*, *122*, 8488–8501. https://doi.org/10.1002/2017JA024389

Hamilton, D. C., Gloeckler, G., Ipavich, F. M., St-demann, W., Wilken, B., & Kremser, G. (1988). Ring current development during the great geomagnetic storm of February 1986. *Journal of Geophysical Research*, *93*(A12), 14,343–14,355. https://doi.org/10.1029/JA093iA12p14343

Hudson, M. K., Baker, D. N., Goldstein, J., Kress, B. T., Paral, J., Toffoletto, F. R., & Wiltberger, M. (2014). Simulated magnetopause losses and Van Allen probe flux dropouts. *Geophysical Research Letters*, *41*, 1113–1118. https://doi.org/10.1002/2014GL059222

Kim, H.-J., & Chan, A. A. (1997). Fully adiabatic changes in storm time relativistic electron fluxes. *Journal of Geophysical Research*, *102*(A10), 22,107–22,116. https://doi.org/10.1029/97JA01814

Kletzing, C., Kurth, W., Acuna, M. M. R., Torbert, R., Averkamp, T., Bodet, D., et al. (2013). The Electric and Magnetic Field Instrument Suite and Integrated Science (EMFISIS) on RBSP. *Space Science Reviews*, *179*(1-4), 127–181. https://doi.org/10.1007/s11214-013-9993-6

Korth, A., Friedel, R., Frutos-Alfaro, F., Mouikis, C., & Zong, Q. (2002). Ion composition of substorms during storm-time and non-storm-time periods space storms and space weather. *Journal of Atmospheric and Solar-Terrestrial Physics*, *64*(5), 561–566. https://doi.org/10.1016/S1364-6826(02)00013-5

Kurth, W., De Pascuale, S., Faden, J., Kletzing, C., Hospodarsky, G., Thaller, S., & Wygant, J. (2015). Electron densities inferred from plasma wave spectra obtained by the waves instrument on Van Allen Probes. *Journal of Geophysical Research: Space Physics*, *120*, 904–914. https://doi.org/

Li, Z. Z., Hudson, M., Kress, B., & Paral, J. (2015). Three-dimensional test particle simulation of the 17–18 March 2013 CME shock-driven storm. *Geophysical Research Letters*, *42*, 5679–5685. https://doi.org/10.1002/2015GL064627

Li, Z. Z., Hudson, M., Paral, J., Wiltberger, M., & Turner, D. (2016). Global ULF wave analysis of radial diffusion coefficients using a global MHD model for the 17 March 2015 storm. *Journal of Geophysical Research: Space Physics*, *121*, 6196–6206. https://doi.org/10.1002/2016JA022508

Li, Z. Z., Hudson, M., Paral, J., Wiltberger, M., Turner, D., & Boyd, A. (2017). ULF wave analysis and radial diffusion calculation using a global MHD model for the 17 March 2013 and 2015 storms. *Journal of Geophysical Research: Space Physics*, *122*, 7353–7363. https://doi.org/10.1002/2016JA023846

Li, Z., Millan, R. M., Hudson, M. K., Woodger, L. A., Smith, D. M., Chen, Y., et al. (2014). Investigation of EMIC wave scattering as the cause for the barrel 17 January 2013 relativistic electron precipitation event: A quantitative comparison of simulation with observations. *Geophysical Research Letters*, *41*, 8722–8729. https://doi.org/10.1002/2014GL062273

Li, W. W., Ni, B., Thorne, R. M., Bortnik, J., Green, J. C., Kletzing, C. A., et al. (2013). Constructing the global distribution of chorus wave intensity using measurements of electrons by the POES satellites and waves by the Van Allen Probes. *Geophysical Research Letters*, *40*, 4526–4532. https://doi.org/10.1002/grl.50920

Li, W. W., Shprits, Y. Y., & Thorne, R. M. (2007). Dynamic evolution of energetic outer zone electrons due to wave-particle interactions during storms. *Journal of Geophysical Research*, *112*(A10220). https://doi.org/10.1029/2007JA012368

Li, W. W., Thorne, R. M., Angelopoulos, V., Bortnik, J., Cully, C. M., Ni, B., et al. (2009). Global distribution of whistler-ode chorus waves observed on the THEMIS spacecraft. *Geophysical Research Letters*, *36*, L09104. https://doi.org/10.1029/2009GL037595

Ma, Q., Li, W., Thorne, R. M., Ni, B., Kletzing, C. A., Kurth, W. S., et al. (2015). Modeling inward diffusion and slow decay of energetic electrons in the Earth's outer radiation belt. *Geophysical Research Letters*, *42*, 987–995. https://doi.org/10.1002/2014GL062977

Meredith, N. P., Horne, R. B., Sicard Piet, A., Boscher, D., Yearby, K. H., Li, W., & Thorne, R. M. (2012). Global model of lower band and upper band chorus from multiple satellite observations. *Journal of Geophysical Research*, *117*, A10225. https://doi.org/10.1029/2012JA017978

Meredith, N. P., Horne, R. B., Thorne, R. M., & Anderson, R. R. (2003). Favored regions for chorus-driven electron acceleration to relativistic energies in the Earth's outer radiation belt. *Geophysical Research Letters*, *30*(16), 1871. https://doi.org/10.1029/2003GL017698

Meredith, N. P., Horne, R. B., Thorne, R. M., Summers, D., & Anderson, R. R. (2004). Substorm dependence of plasmaspheric hiss. *Journal of Geophysical Research*, *109*, A06209. https://doi.org/10.1029/2004JA010387

Meredith, N. P., Thorne, R. M., Horne, R. B., Summers, D., Fraser, B. J., & Anderson, R. R. (2003). Statistical analysis of relativistic electron energies for cyclotron resonance with EMIC waves observed on CRRES. *Journal of Geophysical Research*, *108*(A6), 1250. https://doi.org/10.1029/2002JA009700

Millan, R., & Thorne, R. (2007). Review of radiation belt relativistic electron losses. *Journal of Atmospheric and Solar-Terrestrial Physics*, *69*(3), 362–377. https://doi.org/10.1016/j.jastp.2006.06.019

Millan, R., Yando, K., Green, J., & Ukhorskiy, A. (2010). Spatial distribution of relativistic electron precipitation during a radiation belt depletion event. *Geophysical Research Letters*, *37*, L20103. https://doi.org/10.1029/2010GL044919

Min, K., Liu, K., Bonnell, J., Breneman, A., Denton, R., Funsten, H., et al. (2015). Study of EMIC wave excitation using direct ion measurements. *Journal of Geophysical Research: Space Physics*, *120*, 2702–2719. https://doi.org/10.1002/2014JA020717

Mourenas, D., Artemyev, A. V., Ma, Q., Agapitov, O. V., & Li, W. (2016). Fast dropouts of multi-MeV electrons due to combined effects of EMIC and whistler mode waves. *Geophysical Research Letters*, *43*, 4155–4163. https://doi.org/10.1002/2016GL068921

Orlova, K., Shprits, Y., & Spasojevic, M. (2016). New global loss model of energetic and relativistic electrons based on Van Allen Probes measurements. *Journal of Geophysical Research: Space Physics*, *121*, 1308–1314. https://doi.org/10.1002/2015JA021878

Ozeke, L. G., & Mann, I. R. (2004). Modeling the properties of guided poloidal Alfvén waves with finite asymmetric ionospheric conductivities in a dipole field. *Journal of Geophysical Research*, *109*, A05205. https://doi.org/10.1029/2003JA010151

Ozeke, L. G., Mann, I. R., O'Brien, T. P., Looper, M. D., & Blake, J. B. (2004). Quantification of relativistic electron microburst losses during the GEM storms. *Geophysical Research Letters*, *31*, L04802. https://doi.org/10.1029/2003GL018621

Qin, M., Hudson, M., Millan, R., Woodger, L., & Shekhar, S. (2018). Statistical investigation of the efficiency of EMIC waves in precipitating relativistic electrons. *Journal of Geophysical Research: Space Physics*, *123*, 6223–6230. https://doi.org/10.1029/2018JA025419

Reeves, G. D., McAdams, K. L., Friedel, R. H. W., & O'Brien, T. P. (2003). Acceleration and loss of relativistic electrons during geomagnetic storms. *Geophysical Research Letters*, *30*(10), 1529. https://doi.org/10.1029/2002GL016513

Shen, X.-C., Hudson, M. K., Jaynes, A. N., Shi, Q., Tian, A., Claudepierre, S. G., et al. (2017). Statistical study of the storm time radiation belt evolution during Van Allen Probes era: CME- versus CIR-driven storms. *Journal of Geophysical Research: Space Physics*, *122*, 8327–8339. https://doi.org/10.1002/2017JA024100

Shprits, Y. Y., Drozdov, A. Y., Spasojevic, M., Kellerman, A. C., Usanova, M. E., Engebretson, M. J., et al. (2016). Wave-induced loss of ultra-relativistic electrons in the Van Allen radiation belts. *Nature Communications*, *7*, 12883.

Shprits, Y. Y., Thorne, R. M., Friedel, R., Reeves, G. D., Fennell, J., Baker, D. N., & Kanekal, S. G. (2006). Outward radial diffusion driven by losses at magnetopause. *Journal of Geophysical Research*, *111*, a11214. https://doi.org/10.1029/2006JA011657

Spence, H. E., Reeves, G. D., Baker, D. N., Blake, J. B., Bolton, M., Bourdarie, S., et al. (2013). Science goals and overview of the Radiation Belt Storm Probes (RBSP) Energetic Particle, Composition, and Thermal Plasma (ECT) suite on NASA's Van Allen Probes mission. *Space Science Reviews*, *179*(1), 311–336. https://doi.org/10.1007/s11214-013-0007-5

Su, Z., Gao, Z., Zheng, H., Wang, Y., Wang, S., Spence, H. E., et al. (2017). Rapid loss of radiation belt relativistic electrons by EMIC waves. *Journal of Geophysical Research: Space Physics*, *122*, 9880–9897. https://doi.org/10.1002/2017JA024169

Summers, D., Ni, B., & Meredith, N. (2007). Timescales for radiation belt electron acceleration and loss due to resonant wave-particle interactions: 1. Theory. *Journal of Geophysical Research*, *112*, A04207. https://doi.org/10.1029/2006JA011801

Summers, D., & Thorne, R. (2003). Relativistic electron pitch-angle scattering by electromagnetic ion cyclotron waves during geomagnetic storms. *Journal of Geophysical Research*, *108*(A4), 1143. https://doi.org/10.1029/2002JA009489

Takahashi, K., Ohtani, S.-i., Denton, R. E., Hughes, W. J., & Anderson, R. R. (2008). Ion composition in the plasma trough and plasma plume derived from a Combined Release and Radiation Effects Satellite magnetoseismic study. *Journal of Geophysical Research*, *113*, a12203. https://doi.org/10.1029/2008JA013248

Thorne, R. M., Li, W., Ni, B., Ma, Q., Bortnik, J., Baker, D. N., et al. (2013). Evolution and slow decay of an unusual narrow ring of relativistic electrons near L $\sim$ 3.2 following the September 2012 magnetic storm. *Geophysical Research Letters*, *40*, 3507–3511. https://doi.org/10.1002/grl.50627

Tsyganenko, N. A., & Sitnov, M. I. (2005). Modeling the dynamics of the inner magnetosphere during strong geomagnetic storms. *Journal of Geophysical Research*, *110*, a03208. https://doi.org/10.1029/2004JA010798

Turner, D., Shprits, Y., Hartinger, M., & Angelopoulos, V. (2012). Explaining sudden losses of outer radiation belt electrons during geomagnetic storms. *Nature Physics*, *8*(3), 2185. https://doi.org/10.1038/nphys2185

Usanova, M., Drozdov, A., Orlova, K., Mann, I. R., Shprits, Y., Robertson, M. T., et al. (2014). Effect of EMIC waves on relativistic and ultrarelativistic electron populations: Ground-based and Van Allen Probes observations. *Geophysical Research Letters*, *41*, 1375–1381. https://doi.org/10.1002/2013GL059024

Uzbekov, B., Shprits, Y. Y., & Orlova, K. (2016). Scattering of relativistic and ultra-relativistic electrons by obliquely propagating electromagnetic ion cyclotron waves. *Journal of Atmospheric and Solar-Terrestrial Physics*, *148*, 22–31. https://doi.org/10.1016/j.jastp.2016.08.004

Wilson, L. B., Kersten, C. A., Cattell, P. J., Kellogg, J. R., Wygant, K., Goetz, A., & Breneman, K. (2011). The properties of large amplitude whistler mode waves in the magnetosphere: Propagation and relationship with geomagnetic activity. *Geophysical Research Letters*, *38*, L17107. https://doi.org/10.1029/2011GL048671

Xiang, Z., Tu, W., Li, X., Ni, B., Morley, S., & Baker, D. (2017). Understanding the mechanisms of radiation belt dropouts observed by Van Allen Probes. *Journal of Geophysical Research: Space Physics*, *122*, 9858–9879. https://doi.org/10.1002/2017JA024487

Zhang, X. J., Mourenas, D., Artemyev, A. V., Angelopoulos, V., & Thorne, R. M. (2017). Contemporaneous EMIC and whistler mode waves: Observations and consequences for MeV electron loss. *Geophysical Research Letters*, *44*, 8113–8121. https://doi.org/10.1002/2017GL073886